

Dynamics of steps along a martensitic phase boundary II: numerical simulations

Yubao Zhen,

*School of Astronautics, Harbin Institute of Technology, Harbin, 150001, P.R.
China*

Anna Vainchtein *

Department of Mathematics, University of Pittsburgh, Pittsburgh, PA 15260, USA

Abstract

We investigate the dynamics of steps along a phase boundary in a cubic lattice undergoing antiplane shear deformation. The phase transition is modeled by assuming piecewise linear stress-strain law with respect to one component of the shear strain, while the material response to the other component is linear. In the first part of the paper we have constructed semi-analytical solutions featuring sequential propagation of steps. In this work we conduct a series of numerical simulations to investigate stability of these solutions and study other phenomena associated with step nucleation. We show that sequential propagation of sufficiently small number of steps can be stable, provided that the velocity of the steps is below a certain critical value that depends on the material parameters and the step configuration. Above this value we observe a cascade nucleation of multiple steps which then join sequentially moving groups. Depending on material anisotropy, the critical velocity can be either subsonic or supersonic, resulting in subsonic step nucleation in the first case and steady supersonic sequential motion in the second. The numerical simulations are facilitated with an exact non-reflecting boundary condition and a fast algorithm for its implementation, which are developed to eliminate the possible artificial wave reflection from the computational domain boundary.

Key words: sequential motion, non-reflecting boundary condition, interphase step, supersonic motion, cascade nucleation

* Corresponding author. Tel.: +1 412 624 8309; Fax: +1 412 624 8397.

Email addresses: zhenyb@hit.edu.cn (Yubao Zhen), aav4@pitt.edu (Anna Vainchtein).

1 Introduction

This work is the second part of a two-part paper analyzing the motion of steps along a phase boundary in a cubic lattice undergoing antiplane shear deformation. In the preceding paper (Zhen and Vainchtein, 2007), henceforth referred to as Part I, we introduced the problem and derived semi-analytical solutions for a phase-transforming material with a stress-strain relation that is linear with respect to one component of shear strain and piecewise linear with respect to another. The problem then reduces to solving the system of dimensionless equations

$$\begin{aligned} \frac{d^2 u_{m,n}}{d\tau^2} = & f_h(u_{m+1,n} - u_{m,n}) - f_h(u_{m,n} - u_{m-1,n}) \\ & + f_v(u_{m,n+1} - u_{m,n}) - f_v(u_{m,n} - u_{m,n-1}) \end{aligned} \quad (1)$$

in a square lattice, where the $u_{m,n}(\tau)$ is the antiplane displacement field at time τ . In Eq. (1) the interaction forces for bonds in the horizontal direction (with the strains $w_{m,n} = u_{m,n} - u_{m-1,n}$) are linear:

$$f_h(w) = \chi w, \quad (2)$$

while the vertical bonds (with the strains $v_{m,n} = u_{m,n} - u_{m,n-1}$) are governed by piecewise linear force-strain law:

$$f_v(v) = v - a\theta(|v| - v_c)\text{sgn}(v), \quad (3)$$

with the linear branches representing different material phases. Here $\theta(x)$ is the unit step function. The dimensionless parameter χ in (2) measures the relative strength of the horizontal bonds to that of the vertical ones and thus reflects the degree of anisotropy of the lattice. The other two parameters are the transformation strain $a > 0$, measuring the distance between the adjacent linear branches, and the critical strain $v_c > 0$ separating the different phases. We seek solutions of (1) for a single phase boundary that contains a finite number of steps, or ledges, and investigate the motion of these steps when a constant shearing force is applied at infinity. In Part I we assumed a particular motion ansatz in which the steps move *sequentially*, that is, all steps propagate through the lattice with the same velocity but there are time delays between their motions. Under this assumption we have derived an exact solution, up to the integrals that need to be evaluated numerically, for an arbitrary finite number of steps and have obtained kinetic laws governing the step motion. The asymptotic expressions for the integrals involved in the solution are also derived.

In this part we solve the problem numerically without assuming any particular motion pattern. We show that the solution derived in Part I can be

stable and that multiple solutions of this type with different motion parameters can coexist at the same applied force. For subsonic propagation of two steps, the comparison of numerical and analytical solutions, as well as the lattice anisotropy effect on the kinetic relations are studied in detail and yield an excellent agreement with the theoretical results in Part I. Investigations of the dynamics of multiple steps show stability of sequential motion for at least a sufficiently small number of steps at velocities below a certain critical value. The critical velocity, depending on the material parameters and the step configuration, can be subsonic or supersonic. In particular, we observe a stable supersonic step motion. In addition, the simulations reveal other solutions where sequential motion of a step group coexist with other steps moving with a different speed. In these cases the kinetic laws derived in Part I can still be used if the sequentially moving group is sufficiently isolated.

Our simulations also show that a single step moving with velocity above the critical value gives rise to a cascade nucleation of new steps that then join in sequentially moving groups, all propagating at the same speed. As shown in Part I and verified by the simulations, the value of the critical velocity depends on the anisotropy parameter χ . For $\chi < 2$, the value is subsonic, while a larger χ results in supersonic critical speed.

A difficulty encountered in simulating all lattice defects, such as phase boundaries, ledges, dislocations and cracks is the reflection of lattice waves emitted by the defects from the boundaries of the computational domain. The interaction of the reflected waves with the lattice defects has a significant effect on the defect dynamics (Koizumi et al., 2002). Although in one-dimensional simulations this problem can be avoided by making the computational domain sufficiently large, this solution becomes impractical in higher-dimensional simulations. To resolve this issue, we derive an exact non-reflecting boundary condition and devise a fast algorithm for its implementation. This allows us to compare the numerical solutions to the solutions derived in Part I for an infinite lattice.

The paper is organized as follows. In Section 2 the non-reflecting boundary condition and the fast algorithm for its implementation are derived. The setup for numerical simulations is given in Section 3. Numerical simulations showing stable alternate motion of two steps are presented in Section 4, and the multistep motion is studied in Section 5. The results showing step nucleation are contained in Section 6. We discuss the results and make some concluding remarks in Section 7. Derivation of an equilibrium solution used to obtain initial condition for the simulations can be found in Appendix A.

2 Non-reflecting boundary condition for antiplane shear lattice problem

2.1 *A note on non-reflecting boundary conditions*

The semi-analytical solution in Part I was obtained under the assumption of an infinite lattice. It shows that the propagating steps emit lattice waves with an amplitude that decays very slowly (inverse square-root order) away from the front. Since a numerical simulation is necessarily performed on a bounded domain, the reflection of waves from the boundary will inevitably make the numerical solution different from the one solving the problem in an unbounded lattice. To capture this solution, it is necessary to introduce an artificial boundary condition on the truncated domain, such that the solution on the finite domain is the same as that in the unbounded case. This boundary condition, known as non-reflecting boundary condition (NRBC) and sometimes referred to in the literature as transparent or absorbing boundary condition, has been a long standing research topic in the last three decades. For some recent reviews, see Givoli (1991), Tsynkov (1998), Hagstrom (1999). The classic work of Engquist and Majda (1977, 1979), Bayliss and Turkel (1980) and Higdon (1986, 1990), as well as the celebrated Sommerfeld radiation condition have been widely used. Exact NRBC, known as Dirichlet-to-Neumann map, has been devised for continuous space; see, for example, the work of Grote and Keller (1995a,b) and Givoli (1999). For a one-dimensional discrete harmonic chain, an exact NRBC is given by Adelman and Doll (1974). Cai et al. (2000) propose a time-dependent boundary condition that minimizes the reflection of elastic waves across the boundary by coupling an atomistic simulation system to a linearly elastic surrounding region. Further work on the molecular dynamics simulations on general crystal structures can be found, for example, in Li and E (2006), Karpov et al. (2005), Park et al. (2005), Wagner et al. (2004). Unfortunately, it is well known that in both continuous and discrete problems the exact NRBCs are nonlocal in both space and time. In addition, these boundary conditions are usually constrained to simple geometric boundaries such as sphere, circle, planar surface, etc. Local approximation of the exact-type conditions, either in time and space or both, have been proposed to simplify the implementation. However, given the requirement of accuracy for long-term simulation, exact NRBCs are still of great practical interest. Recently, some new computationally efficient forms of the exact NRBCs have been proposed for three-dimensional continuum problems. For example, Ryaben'kii et al. (2001), propose an algorithm based on the presence of lacunae for three-dimensional wave propagation. A Kirchhoff-type NRBC obtained in Teng (2003) is suitable for an arbitrary artificial boundary, and the computational algorithm limits the temporal nonlocality to a fixed amount of past information.

In this section, we develop an exact NRBC for antiplane shear problem in a cubic lattice. The main feature of our method is that the value on the boundary depends on the history of the boundary itself and the adjacent interior nodes. This leads to a significant reduction of spatial dependence. Moreover, we devise a fast algorithm that completely removes the temporal dependence, hence no history computation and storage are required. The temporal saving is achieved by implementing for each step a primitive operation on an extended spatial domain which can be carried out rapidly with a fixed amount of work.

To derive the NRBC we will use a method closely related to Green's and Kirchhoff's theorems, which can be derived from the reciprocity theorem. The kernel of the method is the lattice Green's function. An introduction to static and time-harmonic lattice Green's functions can be found in Katsura et al. (1971); see also Katsura and Inawashiro (1971), Morita (1971) and Glasser and Boersma (2000), where these functions were computed. However, there appears to be little analytical work for the general time-dependent case, due to the difficulties encountered in evaluating the multiple integrals introduced by the transform method (see Eq. (13)). We note that an inherently different method has been proposed by Tewary (1995) to represent the dynamic Green's function using Radon transform and delta functions, albeit in a three-dimensional continuum problem. Our discrete NRBC can be viewed as a discrete version of the Kirchhoff's theorem.

2.2 NRBC for the antiplane shear lattice problem

Recall that an antiplane shear deformation of a cubic lattice can be viewed as an out-of-plane displacement of a two-dimensional square lattice $\mathbb{L} = \mathbb{Z} \times \mathbb{Z}$. As shown in Fig. 1, we select a sufficiently large artificial boundary \mathcal{S} so that during the time period of interest the phase transformation occurs only in the domain Ω enclosed by the boundary. The displacement field $u_{m,n}(\tau)$ in the lattice can be written as

$$u_{m,n}(\tau) = u_{m,n}^I + u_{m,n}^A(\tau),$$

where $u_{m,n}^I$ is the equilibrium solution given in Appendix A for the initial step configuration. The remaining part $u_{m,n}^A(\tau)$ of the total displacement is the dynamic contribution, and its value in the domain Ω (including its boundary \mathcal{S}) is found from the numerical simulation. In the exterior domain $\mathcal{D} \equiv \mathbb{L} \setminus \Omega$, $u_{m,n}^A(\tau)$ satisfies the (anisotropic) discrete linear wave equation

$$\frac{d^2}{d\tau^2} u_{m,n}^A = \chi(u_{m-1,n}^A + u_{m+1,n}^A) + u_{m,n-1}^A + u_{m,n+1}^A - 2(\chi+1)u_{m,n}^A, \quad (m, n) \in \mathcal{D} \quad (4)$$

with no source term. It also satisfies the homogenous initial conditions

$$u_{m,n}^A(0) = \frac{d}{d\tau}u_{m,n}^A(0) = 0, \quad (m, n) \in \mathcal{D}. \quad (5)$$

Let $\mathcal{S}^+ \subset \mathcal{D}$ be the set of lattice points that have at least one nearest neighbor belonging to \mathcal{S} . We will derive a non-reflecting boundary condition that determines $u_{m,n}^A(\tau)$ at any point in \mathcal{D} in terms of its values on \mathcal{S} and \mathcal{S}^+ .

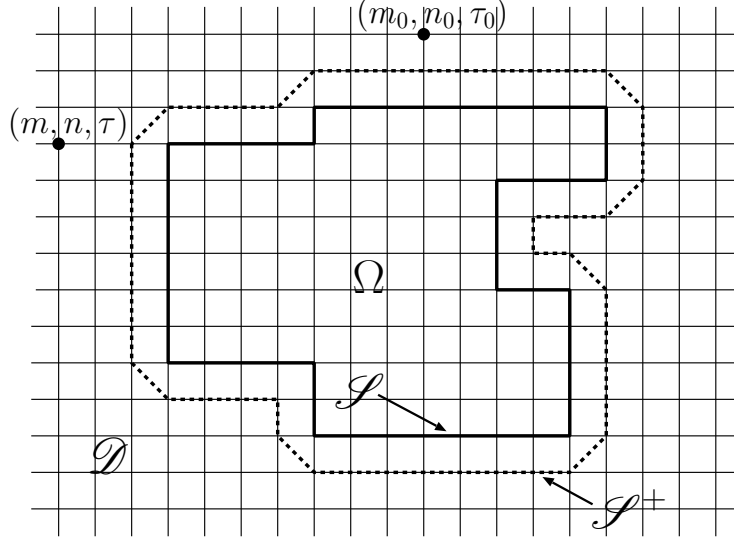


Fig. 1. A two-dimensional unbounded square lattice with an arbitrary artificial boundary \mathcal{S} and the set \mathcal{S}^+ of adjacent lattice points. The boundary \mathcal{S} is selected so that the phase transitions only occur in the interior domain Ω during the time period of interest.

We now introduce the time-dependent lattice Green's function $\mathcal{G}_{m,n|m_0,n_0}(\tau, \tau_0)$ that satisfies the discrete linear wave equation with a Dirac source term:

$$\begin{aligned} \frac{\partial^2}{\partial \tau^2} \mathcal{G}_{m,n} = & \chi(\mathcal{G}_{m-1,n} + \mathcal{G}_{m+1,n}) + \mathcal{G}_{m,n-1} + \mathcal{G}_{m,n+1} - 2(\chi + 1)\mathcal{G}_{m,n} \\ & + \delta_{m,m_0} \delta_{n,n_0} \delta(\tau - \tau_0), \quad (m, n), (m_0, n_0) \in \mathbb{L}. \end{aligned} \quad (6)$$

Here $\delta_{i,j}$ denotes the Kronecker delta function and $\delta(t)$ is the Dirac delta function. In Eq. (6) only moving indices are shown, with a fixed source position (m_0, n_0) . In addition, \mathcal{G} is required to satisfy the conditions

$$\mathcal{G}_{m,n}(\tau, \tau^+) = \frac{\partial}{\partial \tau_0} \mathcal{G}_{m,n}(\tau, \tau^+) = 0 \quad (7)$$

at some time $\tau^+ > 0$. Due to its invariance with respect to translation in space and time, the Green's function $\mathcal{G}_{m,n|m_0,n_0}(\tau, \tau_0)$ has the following reciprocity property:

$$\mathcal{G}_{m,n|m_0,n_0}(\tau, \tau_0) = \mathcal{G}_{m_0,n_0|m,n}(-\tau_0, -\tau) = \mathcal{K}_{m-m_0, n-n_0}(\tau - \tau_0), \quad (8)$$

where the nonlocal history kernel $\mathcal{K}_{m,n}(\tau)$ is introduced for later use. Indeed, after making the replacements $m \leftrightarrow m_0$, $n \leftrightarrow n_0$, $\tau \leftrightarrow (-\tau_0)$, one can see that Eq. (6) is still valid with space-time basis changing to (m_0, n_0, τ_0) :

$$\begin{aligned} \frac{\partial^2}{\partial \tau_0^2} \mathcal{G}_{m_0, n_0} = & \chi(\mathcal{G}_{m_0-1, n_0} + \mathcal{G}_{m_0+1, n_0}) + \mathcal{G}_{m_0, n_0-1} + \mathcal{G}_{m_0, n_0+1} - 2(\chi + 1)\mathcal{G}_{m_0, n_0} \\ & + \delta_{m, m_0} \delta_{n, n_0} \delta(\tau - \tau_0). \end{aligned} \quad (9)$$

Note that in Eqs. (6) and (9) $\mathcal{G}_{m,n}$ and \mathcal{G}_{m_0, n_0} denote the same quantity $\mathcal{G}_{m,n|m_0, n_0}(\tau, \tau_0)$, but only the moving indices are shown in each equation. That is, in both equations, the source is at (m_0, n_0, τ_0) , and the observer is at (m, n, τ) , but in Eq. (6) the source is fixed and the observer is moving, and in Eq. (9) the source is moving and the observer is fixed.

Similarly, we can rewrite Eq. (4) in the space-time basis (m_0, n_0, τ_0) , obtaining

$$\frac{d^2}{d\tau_0^2} u_{m_0, n_0}^A = \chi(u_{m_0-1, n_0}^A + u_{m_0+1, n_0}^A) + u_{m_0, n_0-1}^A + u_{m_0, n_0+1}^A - 2(\chi + 1)u_{m_0, n_0}^A \quad (10)$$

for $(m_0, n_0) \in \mathcal{D}$.

Following the standard procedure in reciprocity theorem, we multiply Eq. (10) by $\mathcal{G}_{m,n|m_0, n_0}(\tau, \tau_0)$ and subtract Eq. (9) multiplied by $u_{m_0, n_0}^A(\tau_0)$. Summing over (m_0, n_0) in \mathcal{D} and integrating in τ_0 over the time interval $[0, \tau^+]$, we obtain

$$\begin{aligned} & \sum_{(m_0, n_0) \in \mathcal{D}} \left(\frac{d}{d\tau_0} u_{m_0, n_0}^A(\tau_0) \mathcal{G}_{m,n|m_0, n_0}(\tau, \tau_0) - \frac{\partial}{\partial \tau_0} \mathcal{G}_{m,n|m_0, n_0}(\tau, \tau_0) u_{m_0, n_0}^A(\tau_0) \right) \Big|_{\tau=0}^{\tau=\tau^+} \\ & = \int_0^{\tau^+} \sum_{(m_0, n_0) \in \mathcal{D}} \left[\Sigma_{u^A}(m_0, n_0, \tau_0) \mathcal{G}(\tau_0) - \Sigma_{\mathcal{G}}(m_0, n_0, \tau_0) u^A(\tau_0) \right] d\tau_0 - u_{m,n}^A(\tau), \end{aligned}$$

where $\Sigma_u(m, n, \tau) \equiv \chi(u_{m-1, n}(\tau) + u_{m+1, n}(\tau)) + u_{m, n-1}(\tau) + u_{m, n+1}(\tau)$ denotes the weighted sum of $u(\tau)$ over the four nearest neighbors of (m, n) . The left hand side of the above equation vanishes due to the initial conditions (5) and (7). The summation in the first term on the right hand side reduces to a summation over \mathcal{S} and \mathcal{S}^+ due to cancellations. Hence we have

$$\begin{aligned} u_{m,n}^A(\tau) = & \int_0^{\tau^+} \sum_{(m_0, n_0) \in \mathcal{S}^+} \sum_{(i,j) \in \mathcal{S}_N(m_0, n_0)} \beta_{\mathcal{S}}(i, j) \left[\mathcal{G}_{m,n|m_0, n_0}(\tau, \tau_0) u_{i,j}^A(\tau_0) \right. \\ & \left. - u_{m_0, n_0}^A(\tau_0) \mathcal{G}_{m,n|i,j}(\tau, \tau_0) \right] d\tau_0, \quad (m, n) \in \mathcal{D}. \end{aligned} \quad (11)$$

Here $\mathcal{S}_N(m_0, n_0) \equiv \{(i, j) \in \mathcal{S} : |i - m_0| + |j - n_0| \leq 1\}$ is the set of nearest

neighbors of a point $(m_0, n_0) \in \mathcal{S}^+$ that lie on \mathcal{S} , and

$$\beta_{\mathcal{S}}(i, j) = \begin{cases} 1 & \text{if } i = m_0, \\ \chi & \text{if } j = n_0, \end{cases} \quad (i, j) \in \mathcal{S}_N(m_0, n_0). \quad (12)$$

Equation (11) is the general formula for the displacement at any point $(m, n) \in \mathcal{D}$ (note that this includes \mathcal{S}^+). As an important feature, Eq. (11) shows that the displacement at any point in the domain \mathcal{D} is fully determined by the history of the displacement field only at the points on the two sets \mathcal{S} and \mathcal{S}^+ . For $(m, n) \in \mathcal{S}^+$, we then obtain a relation describing the dependence of the dynamic part of the displacement field on \mathcal{S}^+ on the displacement of the points on \mathcal{S}^+ itself and on \mathcal{S} . No other points are needed. This can be viewed as an exact NRBC. Coupled with the contribution to the displacement field due to the phase transition in the interior domain Ω , it eliminates the spurious reflection on the artificial boundary \mathcal{S} .

2.3 Fast algorithm for evaluation of NRBC

Unfortunately, direct use of Eq. (11) is not efficient in practice. If the total number of time steps is N_τ and \mathcal{S}^+ consists of N_s points, the total multiplication operation is of the order $\mathcal{O}(N_s^2 N_\tau^2)$. In fact, the computation gets increasingly slower as it proceeds. In addition, there is an increase of storage requirement due to the history data. Recently Lubich and Schädle (2002) have proposed an elegant fast algorithm to address the problems of this type. Their basic idea is to construct an approximation to the history kernel with a sum of exponential functions. The convolution term can then be shown to satisfy a simple ODE, which can be evaluated by advancing step by step. The implementation of their algorithm relies on two factors: first, the availability of an explicit Laplace transform of the history kernel, and second, the numerical evaluation of the inverse Laplace transform using a Talbot contour. However, there is no analytical result for the Laplace transform of our history kernel $\mathcal{K}_{m,n}(\tau)$ defined in Eq. (8). The transform is given by

$$\tilde{\mathcal{K}}_{m,n}(s) = \frac{1}{\pi^2} \int_0^\pi \int_0^\pi \frac{\cos k_x m \cos k_y n}{s^2 + 2(\chi + 1) - 2(\chi \cos k_x + \cos k_y)} dk_x dk_y, \quad (13)$$

where s is the Laplace transform variable. Although it can be evaluated numerically for given s , it is relatively expensive for computation considering the possible singularities of the integrand. Moreover, Murli and Rizzardi (1990) have shown that results of Talbot's method may be unpredictable for functions with delay, such as our kernel. Due to these difficulties, we devise in this paper a new fast algorithm that requires no such approximation. Similar to other fast algorithms, it requires no storage of the history data.

We note that the basic ingredient of formula (11) is the following convolution:

$$\psi_{m,n|m_0,n_0}^{i,j}(\tau) = \int_0^{\tau^+} \mathcal{K}_{m-m_0,n-n_0}(\tau - \tau_0) u_{i,j}^A(\tau_0) d\tau_0, \quad (14)$$

where the index pair (i, j) takes values on \mathcal{S} and \mathcal{S}^+ . Differentiating Eq. (14) twice with respect to τ and observing that $\mathcal{K}(\tau - \tau^+) = \mathcal{K}'(\tau - \tau^+) = 0$ due to the initial conditions (7), we have

$$\frac{d^2}{d\tau^2} \psi_{m,n|m_0,n_0}^{i,j}(\tau) = \int_0^{\tau^+} \frac{d^2}{d\tau_0^2} \mathcal{K}_{m-m_0,n-n_0}(\tau - \tau_0) u_{i,j}^A(\tau_0) d\tau_0. \quad (15)$$

Along with equations (8), (9) and (14), this implies that

$$\frac{d^2}{d\tau^2} \psi_{m,n|m_0,n_0}^{i,j}(\tau) = \Sigma_{\psi^{i,j}}(m_0, n_0, \tau) - 2(\chi + 1) \psi_{m,n|m_0,n_0}^{i,j}(\tau) + \delta_{m,m_0} \delta_{n,n_0} u_{i,j}^A(\tau), \quad (16)$$

i.e., $\psi_{m,n|m_0,n_0}^{i,j}(\tau)$ itself satisfies a discrete wave equation with respect to spatial indices (m_0, n_0) , with the source $u_{i,j}^A(\tau)$ located at (m, n) . This suggests that we can avoid the computation of the temporal integral in Eq. (14) entirely, and instead solve Eq. (16) directly for $\psi_{m,n|m_0,n_0}^{i,j}(\tau)$. This replaces the temporal nonlocality by the spatial one and eliminates the need to store time history data. Note that

$$\psi_{m,n|m_0,n_0}^{i,j}(\tau) = \psi_{m-m_0,n-n_0|0,0}^{i,j}(\tau) \equiv \Psi(m - m_0, n - n_0, \tau | i, j). \quad (17)$$

Recalling Eq. (11), we can now write the non-reflecting boundary condition as

$$u_{m,n}^A(\tau) = \sum_{(m_0,n_0) \in \mathcal{S}^+} \sum_{(i,j) \in \mathcal{S}_N(m_0,n_0)} \beta_{\mathcal{S}}(i, j) \left[\Psi(m - m_0, n - n_0, \tau | i, j) - \Psi(m - i, n - j, \tau | m_0, n_0) \right], \quad (m, n) \in \mathcal{S}^+. \quad (18)$$

Note that all $u_{m,n}^A(\tau)$ on \mathcal{S}^+ can be computed in a single operation with all the u^A sources switched between \mathcal{S} and \mathcal{S}^+ with the weight $\beta_{\mathcal{S}}$ defined in Eq. (12), followed by a sign change of all the newly switched sources located on the original boundary \mathcal{S} , i.e., change the sign only when values are switched from \mathcal{S}^+ to \mathcal{S} . This primitive operation is the kernel of our fast algorithm.

The operation is implemented using the velocity Verlet molecular dynamics (MD) scheme to solve Eq. (16), on an extended domain covering Ω in all directions with an extra buffer of size N_c around the domain. Zero boundary condition is used on the extended domain. Since the height of the domain Ω used in our simulations is small compared to its length, a $N_c = \mathcal{O}(N_s/2)$ is chosen, so that the cost of the primitive operation is in an order of $\mathcal{O}(6N_c^2) \approx \mathcal{O}(N_s^2)$.

The operation is advanced step by step, requiring no convolution computation and history storage. In addition, the cost per step is independent of time. In comparison to the $\mathcal{O}(N_s^2 N_\tau^2)$ expense of using Eq. (11) directly, the proposed fast algorithm has a reduced expense of $\mathcal{O}(N_s^2 N_\tau)$. This enables the computation on a larger domain and for a longer time.

To test the fast NRBC algorithm, we compute the time-dependent lattice Green’s function itself at $\chi = 1$ for $\tau \in [0, 20]$, first using the velocity Verlet MD scheme with time step 10^{-3} on a square of 200×200 . The fast NRBC algorithm is then tested on a 6×6 square, using $N_c = 50$ for the relevant primitive operation. In both cases, the initial displacement is set to zero and the initial velocity field equals 1 at the center and zero elsewhere. In Fig. 2, the absolute difference between the results from these two methods are depicted at two time instances $\tau = 10$ and $\tau = 20$. Note that at both time instances the wave fronts have already passed through the 6×6 square grid boundary. The results show an excellent agreement.

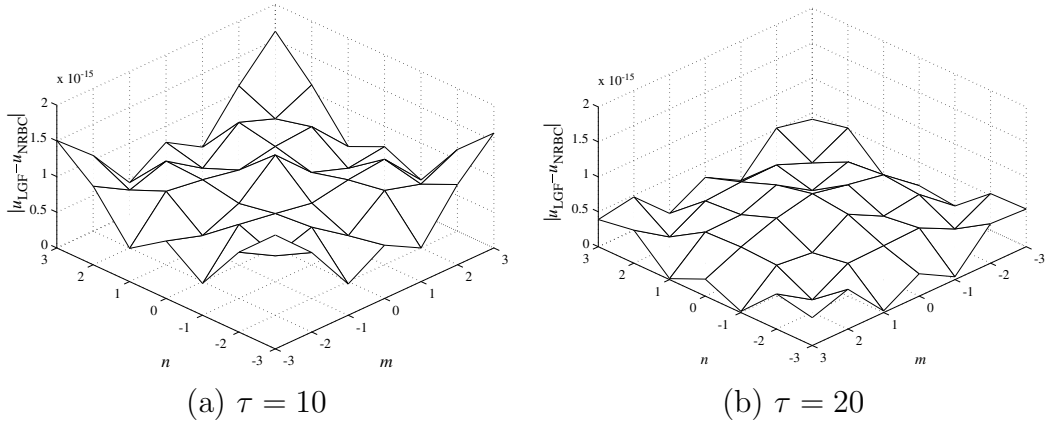


Fig. 2. Two time snapshots of the absolute difference $|u_{\text{LGF}} - u_{\text{NRBC}}|$ between the values of time-dependent lattice Green’s function (LGF) computed directly on a large domain and using the non-reflecting boundary condition with the fast algorithm implemented. Here $\chi = 1$.

3 Setup for numerical simulations

We now describe the setup for the numerical solution of Eq. (1) under applied driving force G . The initial configuration consists of a single phase boundary separating phase II ($v_{m,n} > v_c$) below it from phase I ($|v_{m,n}| < v_c$) above and containing a finite number of steps. We require that far behind the phase boundary the horizontal bonds are undeformed and the vertical bonds remain in phase II, so that the driving force is given by $G = a(v_- - v_c - a/2)$, where v_- is the constant far-field strain in phase II region. As described in Appendix A,

for G below the Peierls force G_P ($v_- < v_-^P$), we obtain an equilibrium configuration with a given distribution of steps. Initial condition for the simulation is then obtained by perturbing the strain in the vertical spring in front of the highest step slightly above the critical value. For $G_P < G < a^2/2$, such equilibrium configuration does not exist, and we start with a non-equilibrium state that has a single phase boundary with a prescribed step geometry and satisfies the equilibrium equations in \mathcal{D} , as required by the procedure we used to obtain the non-reflecting boundary condition.

The numerical simulation is then implemented as follows:

- (1) Set up the initial displacement $u_{m,n}^I$ as described above. The initial velocity is zero.
- (2) Update the displacement field in the interior domain Ω including the boundary \mathcal{S} using the velocity Verlet MD scheme.
- (3) Update the dynamic part $u_{m,n}^A(\tau)$ of the displacement field on \mathcal{S}^+ using the fast NRBC (18). Then update the total displacement $u_{m,n}(\tau) = u_{m,n}^A(\tau) + u_{m,n}^I$.
- (4) Update the velocity field in the interior domain Ω including \mathcal{S} as required in the MD scheme;
- (5) Go back to Step 2.

Unless otherwise stated, all simulations are performed with the following material parameters: $\chi = 1$, $a = 0.22$ and $v_c = 0.42$. Numerical time step is set to $\Delta\tau = 10^{-3}$. In all cases, the characteristic motion parameters are obtained by averaging over 10 contiguous periods near the end of each simulation.

4 Alternate motion of two steps

In this section we describe the numerical simulations showing alternate propagation of two steps. As in Part I, we use the following parameters to characterize the motion of the steps: μ , the distance between the two steps at the start of each motion period, V , the velocity of each step and T_1 , the time delay between the advancement of the first (lower) with respect to the second (upper) step. Recall also that the parameters μ and T_1 can be combined in one, $\alpha = \mu + 1 - T_1V$, the dynamic separation between the two steps. Since μ is an integer and $T_1V < 1$, α uniquely determines $\mu = \lfloor \alpha \rfloor$ (its integer part) and T_1 for given V .

4.1 Subsonic motion

We begin with the case $V < c$, where $c = \sqrt{\chi}$ is the speed of elastic shear waves in the direction of the step motion.

Figure 3 shows the results of the simulation with $v_- = 0.57$ on a 400×8 computational domain. The initial configuration consists of a phase boundary

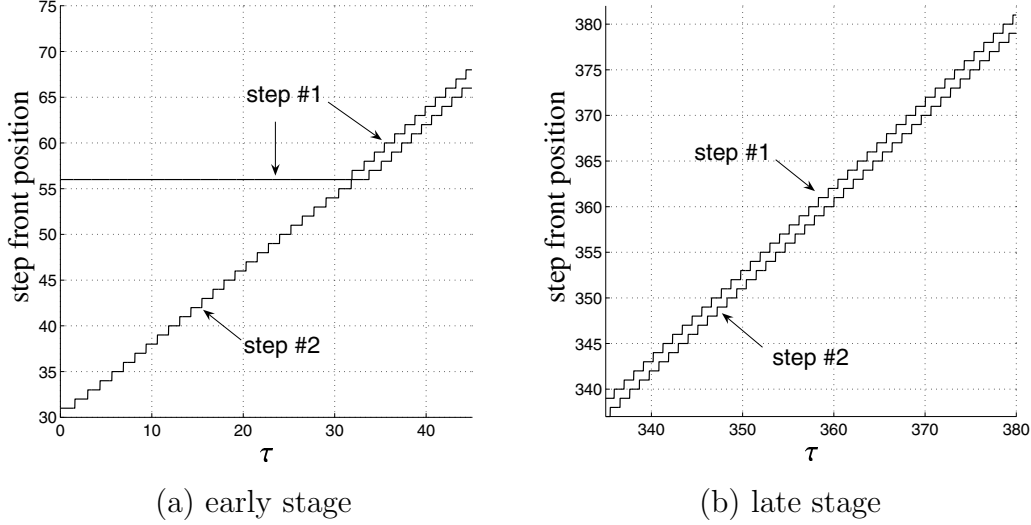


Fig. 3. The alternate motion of a two-step configuration with $v_- = 0.57$. The steady motion has a velocity of $V/c = 0.9395$.

with two steps placed 26 lattice units apart. At the start of the simulation, only the second (upper) step moves until it reaches the first (lower) step. After that, both steps propagate in an alternate way. After an initial transient period, the motion of the steps becomes steady with $V/c = 0.9395$ and $\alpha = 1.5829$.

For comparison, the kinetic relations obtained from the semi-analytical solution and depicted in Figs. 5 and 6 of Part I predict $V/c = 0.94$ and $\alpha = 1.5873$ for a two-step configuration with $\mu = 1$ and $v_- = 0.57$ ($G/a^2 = 0.18$). The snapshots of strain profiles generated by the numerical (squares) and semi-analytical (solid dotted line) solutions across both steps at $\tau = 374.92$ are compared in Figs. 4 and 5 for step #2 and #1, respectively. The time instance is chosen so that the step #2 has just moved to its next position.

The excellent agreement of the numerical simulation results and the theoretical predictions suggests that at these parameter values the alternate motion considered in Part I is stable. We now consider some particular aspects of the two-step subsonic motion.

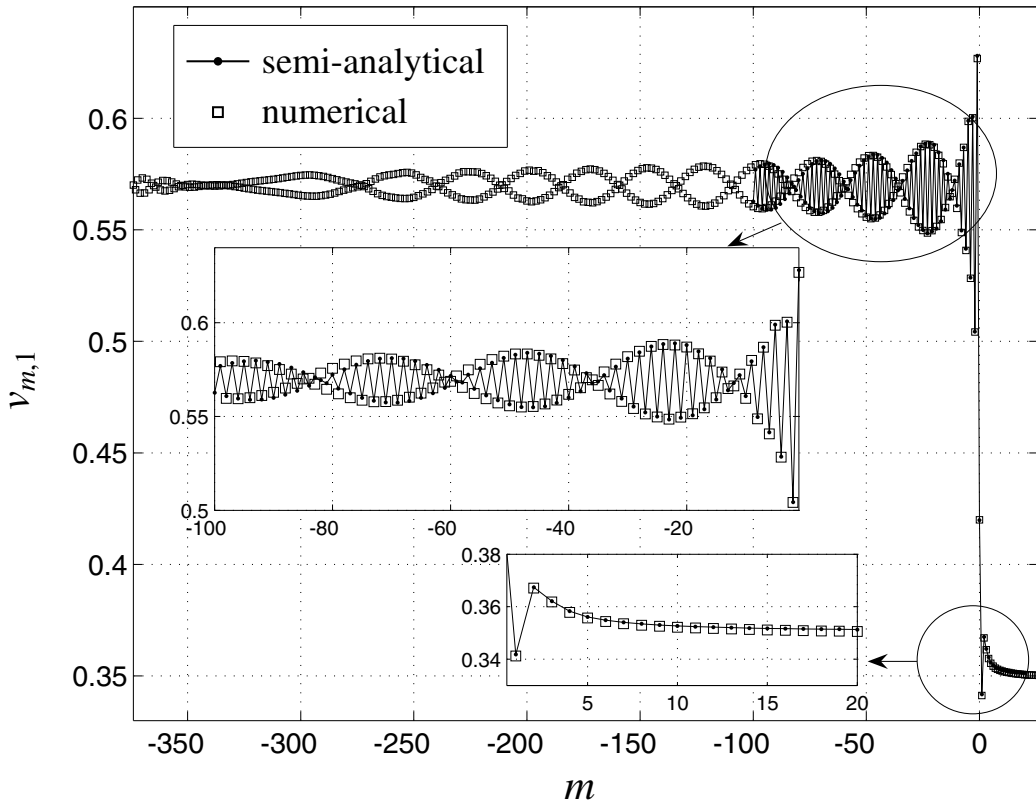


Fig. 4. Comparison of strain profile snapshots across step #2 from numerical simulation and semi-analytical solution at $\tau = 374.92$ and $v_- = 0.57$.

4.2 Lattice waves

Similar to other defects propagating through a non-dissipative lattice, the moving steps emit lattice waves. As predicted in Part I, when steps propagate sufficiently fast (as in the above example), the lattice waves are emitted only in the wake of the moving front.

To show the structure of the lattice waves, it is convenient to introduce the excess vertical strain field

$$v_{m,n}^e(\tau) = v_{m,n}(\tau) - v_{m,n}(0), \quad (19)$$

which measures the change of the vertical strain during the simulation. Since there are no phase changes outside the step zone, we expect only small oscillations of the excess strain field due to the outgoing waves emitted by the moving front. Figure 6 depicts the excess strain profile at $\tau = 380$ for the simulation described above. Notice the V-shaped wave profile and the beats structure predicted in Part I.

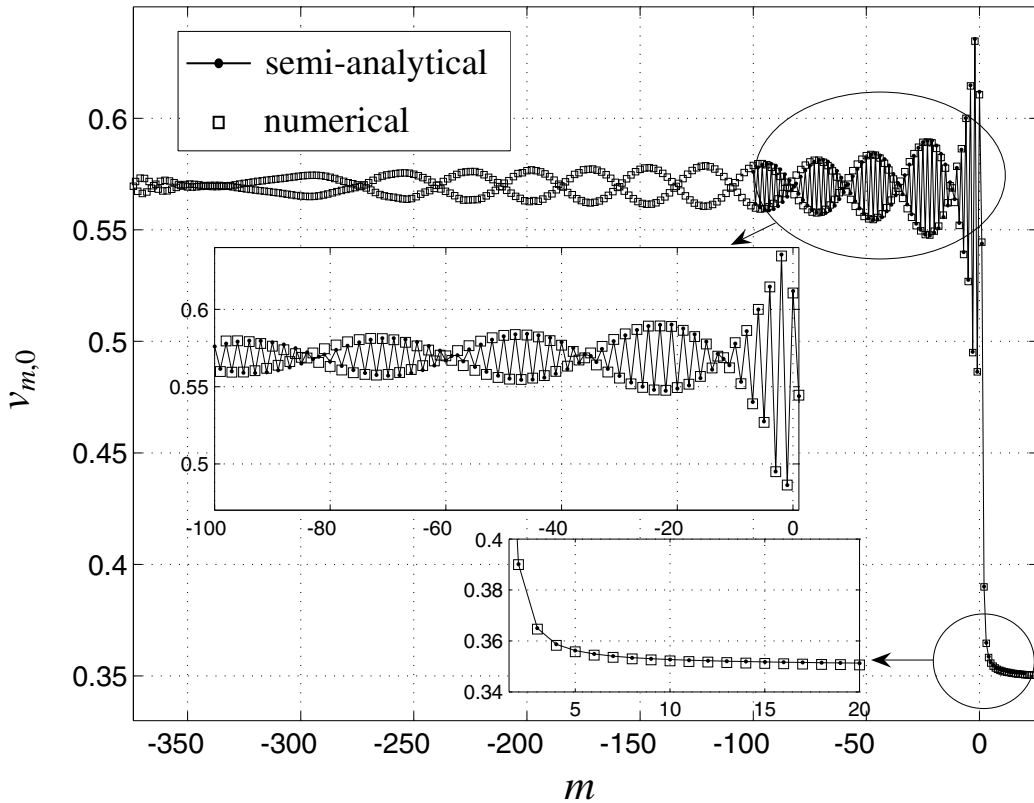


Fig. 5. Comparison of strain profile snapshots across step #1 from numerical simulation and semi-analytical solution at $\tau = 374.92$ and $v_- = 0.57$.

4.3 *Supersonic motion*

Analysis in Part I predicts existence of supersonic solutions exhibiting alternate motion, provided that the velocity is less than a certain critical value V_H depending on χ and the particular solution branch. Our numerical investigation verifies that such supersonic steady alternate motion does exist; see Fig. 7 for two such examples at $\chi = 2$ and 4. As predicted in Part I, the steps tend to be more separated at higher χ . Note also that although the velocity is supersonic, it is very close to the sound speed.

4.4 *Multiplicity, anisotropy and stability of alternate motion*

Analysis in Part I showed that multiple solutions with alternate step motion may coexist at the same velocity or driving force. The multiple solution branches obtained in Part I are shown by solid lines in Fig. 8. To investigate stability of these multiple solutions, we conducted a series of numerical simulations with different initial conditions and applied loadings. The results of the simulations are summarized in Table 1 and shown by circles in Fig. 8.

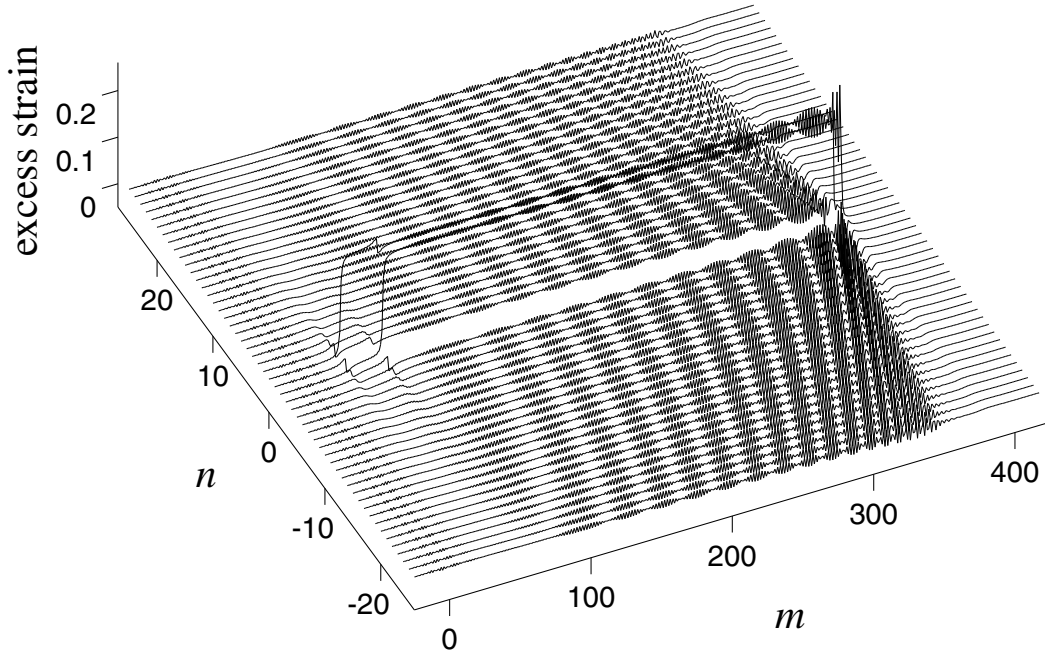


Fig. 6. The excess vertical strain for a two-step configuration moving with $V/c = 0.9395$ at $\tau = 380$. The other parameters are $v_- = 0.57$, $\chi = 1$ and $\alpha = 1.5829$. The data is the same as in Fig. 3.

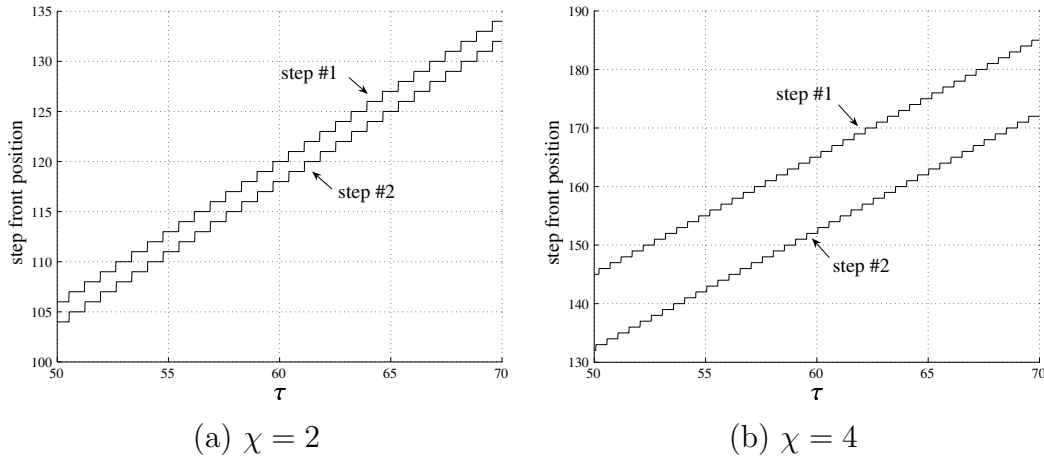


Fig. 7. Supersonic steady alternate motion of two steps. (a) at $\chi = 2$ with $V/c = 1.0021$. Here $v_- = 0.589$ and $\alpha = 2.0221$. (b) at $\chi = 4$ with $V/c = 1.0022$. Here $v_- = 0.59$ and $\alpha = 12.7234$.

Note that all simulations fall onto the odd-numbered branches of the kinetic relation obtained from the theoretical solution. This suggests that the odd-numbered branches contain stable solutions, while the solutions along even-

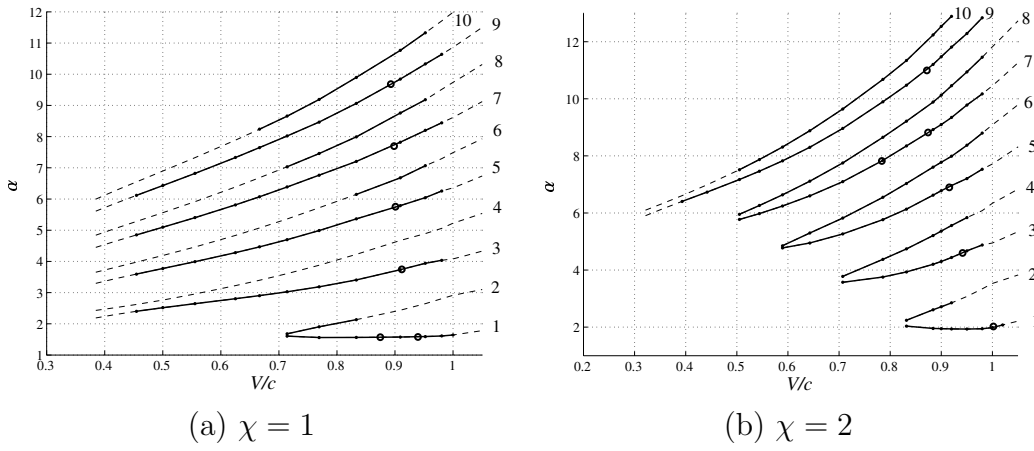


Fig. 8. Relation of α versus V/c from simulation results (circles) with different χ , v_- and initial conditions against the theoretical solution branches (solid lines). All simulations fall onto the odd-numbered branches. Dashed lines indicate non-admissible solutions.

Table 1

Simulation results for a two-step configuration

| $\chi = 1$ | | | | $\chi = 2$ | | | |
|------------|-------|--------|----------|------------|-------|--------|----------|
| v_- | μ | V/c | α | v_- | μ | V/c | α |
| 0.56 | 1 | 0.8747 | 1.5723 | 0.55 | 7 | 0.7838 | 7.8204 |
| 0.57 | 1 | 0.9395 | 1.5829 | 0.56 | 8 | 0.8742 | 8.8170 |
| 0.57 | 3 | 0.9118 | 3.7456 | 0.56 | 10 | 0.8718 | 10.9975 |
| 0.57 | 5 | 0.9009 | 5.7568 | 0.567 | 6 | 0.9157 | 6.8977 |
| 0.57 | 7 | 0.8982 | 7.6982 | 0.57 | 4 | 0.9414 | 4.5979 |
| 0.57 | 9 | 0.8929 | 9.6786 | 0.589 | 2 | 1.0021 | 2.0221 |

numbered branches are unstable.

To see why this may be the case, we recall that the condition derived in Part I for the separation α is $\mathcal{F}(\alpha) = 0$, where we defined

$$\mathcal{F}(\alpha) \equiv g_1(\alpha) - g_1(-\alpha), \quad \alpha \geq 0, \quad (20)$$

with the function g_1 for a given V introduced in Eq. 44 of Part I. Following Flytzanis et al. (1974) in a similar analysis of the motion of two dislocations on the same slip plane, we may interpret the function $\mathcal{F}(\alpha)$ as the mutual force of interaction between the steps. As shown in Fig. 9, the interaction force is repulsive at small $\alpha > 0$ and changes sign as it oscillates at larger α . The non-zero roots of $\mathcal{F}(\alpha)$ correspond to step separations α that lie on different branches of the kinetic relation $\alpha = \alpha(V)$ at the given V . At odd-numbered roots we have $\mathcal{F}'(\alpha) < 0$, and thus the interaction force becomes attractive if the separation between the steps is slightly increased and repulsive if the

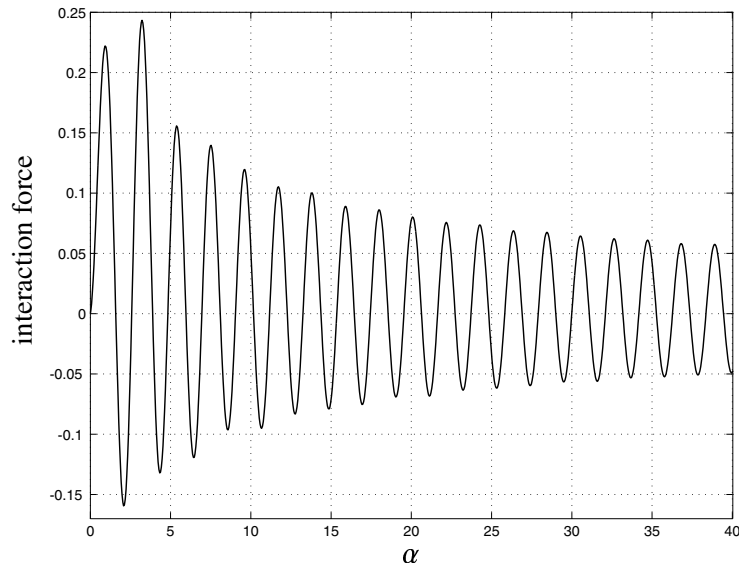


Fig. 9. The step interaction force $\mathcal{F}(\alpha)$ at $V = 0.9395$ and $\chi = 1$.

separation is decreased. Hence we expect the dynamic solutions that lie on odd-numbered branches to be stable. In contrast, a small increase of the step separation away from even-numbered roots (where $\mathcal{F}'(\alpha) > 0$) results in a repulsive interaction force, so that the separation will further grow. Similarly, a small decrease of the separation would yield a further decrease. Hence, we expect the even-numbered branches to contain unstable solutions. This explains why these solutions were not observed in the numerical simulations.

The data from Table 1 also point to several other interesting observations. The first one concerns the effect of anisotropy measured in our problem by the parameter χ . At the same external loading (same v_- or G), a higher χ may result in a larger velocity and a larger separation between the steps. The results also show that depending on the initial condition, there may exist multiple step separations with the same external loading and χ . Finally, observe that at the same χ and external loading smaller step separation leads to a slightly faster motion of the steps.

Our simulations also show that at external loading below a certain threshold that decreases as χ grows, no alternate motion is observed, in agreement with the predictions of Figs. 6, 8 and 9 in Part I. Instead, the higher step propagates a certain distance and stops when the system reaches a stable equilibrium state.

5 Sequential motion of multiple steps

In this section we consider subsonic motion of three and more steps. To describe sequential motion we use the notation introduced in Part I: the N th step is always the highest step, and μ_j denotes the distance between $(N - j)$ th step and N th step after the N step has advanced. For example, if $N = 3$, μ_1 is the distance between the third and second step after the third step has moved, and μ_2 is the distance between the first and third steps. Parameter $T_j < 1/V$ denotes the time delay of the j th step with respect to the N th step.

We start with a three-step configuration. As in the two-step case, only the third (highest) step moves initially. When it reaches the second step, the two steps start moving in an alternate style, while the first one is still motionless. When the second step reaches the first, the first step also starts moving, and all three steps now move sequentially with $\mu_1 = 1$, $\mu_2 = 2$, $V/c = 0.9533$, $T_2 = 0.674$ and $T_1 = 0.088$. See Fig. 10.

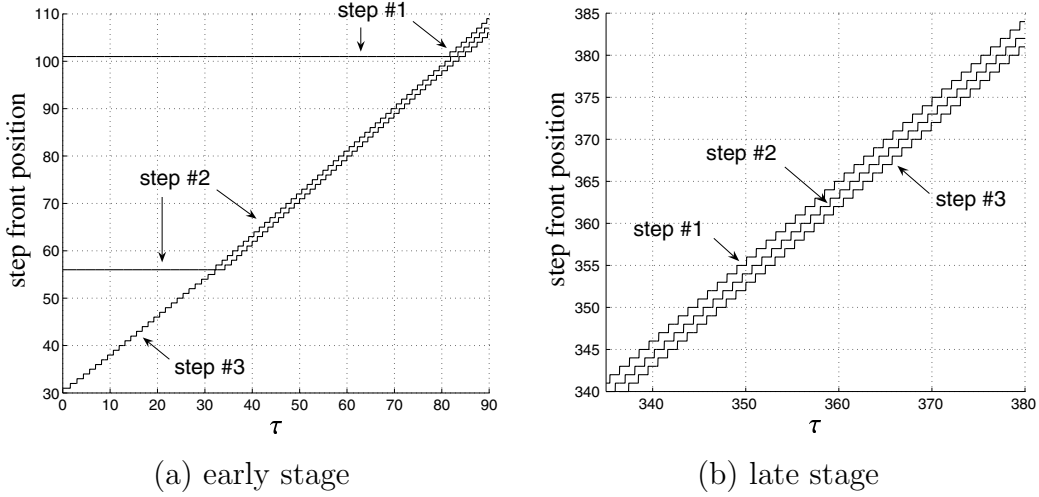


Fig. 10. The sequential motion of a three-step configuration with $v_- = 0.57$ on a computational domain of 400×9 . The steady motion has a velocity of $V/c = 0.9533$.

A comparison of the strain profiles generated by the semi-analytical solution derived in Part I and the above numerical simulation is shown in Fig. 11. The values of separation parameters α_1 and α_2 used in the semi-analytical solution are taken from the numerical simulations. The excellent agreement of the strain profiles indicates stability of the sequential motion at these parameter values.

Figure 12 depicts the motion of a four-step configuration on a computational domain of 400×10 . After some time, the four steps move sequentially with the parameters $\mu_1 = 3$, $\mu_2 = 5$, $\mu_3 = 6$, $V/c = 0.9575$, $T_3 = 0.14$, $T_2 = 0.842$ and $T_1 = 0.26$. Observe that the steps are not uniformly spaced, and the spacing

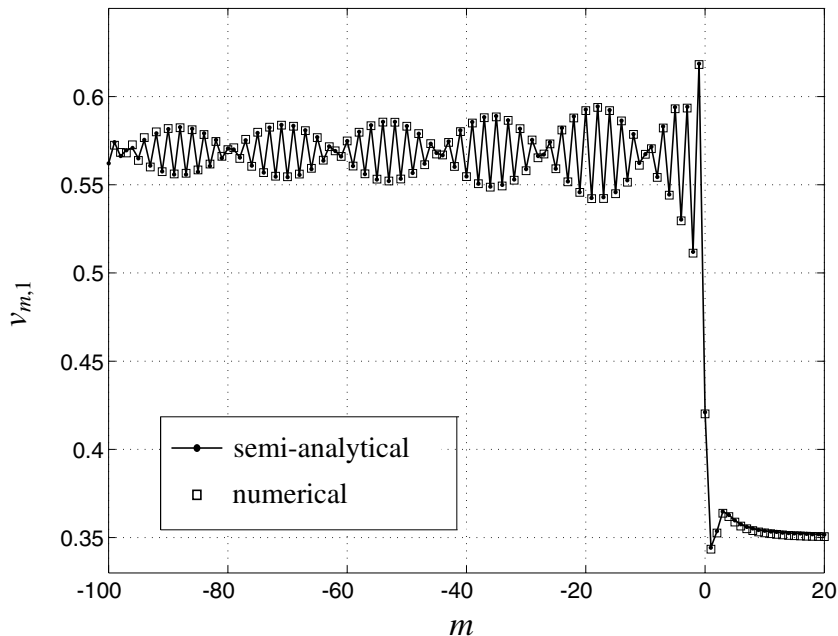


Fig. 11. Comparison of strain profile snapshots across step #3 from a three-step configuration between numerical simulation and semi-analytical solution at $\tau = 359.44$ and $v_- = 0.57$.

between some of the neighboring steps (third and fourth) is not necessarily one lattice unit. Note also that during each time period $T = 1/V$ the order of step advancement (4, 3, 1, 2) does not coincide with the reverse step order.

The late stage of a five-step motion (on a computational domain of 400×11) is shown Fig. 13. In this case steps #1, #2, #3 and #4 form a sequentially moving subgroup with the following characteristic motion parameters (with respect to step #4): $\mu_1 = 1$, $\mu_2 = 2$, $\mu_3 = 4$, $V/c = 0.9615$, $T_3 = 0.42$, $T_2 = 0.142$ and $T_1 = 0.606$. However, step #5 lags behind the subgroup, moving with the different velocity $V_5/c = 0.9183$. This suggests the existence of a large variety of dynamic regimes in which subsonic sequential motion of certain step subgroups coexists with other steps moving at a different speed. We note that if a sequentially moving step group is sufficiently isolated from the other steps, the kinetic relations obtained in Part I can still be used to describe the motion of this group.

Our simulations suggest that as the number of sequentially moving steps increases, so does the velocity of the steps. For example, at $v_- = 0.57$, $\chi = 1$ and similar separations between the steps, the velocity of two, three and four steps moving sequentially are 0.9395, 0.9533 and 0.9575, respectively. The mechanism for this size effect is not yet clear.

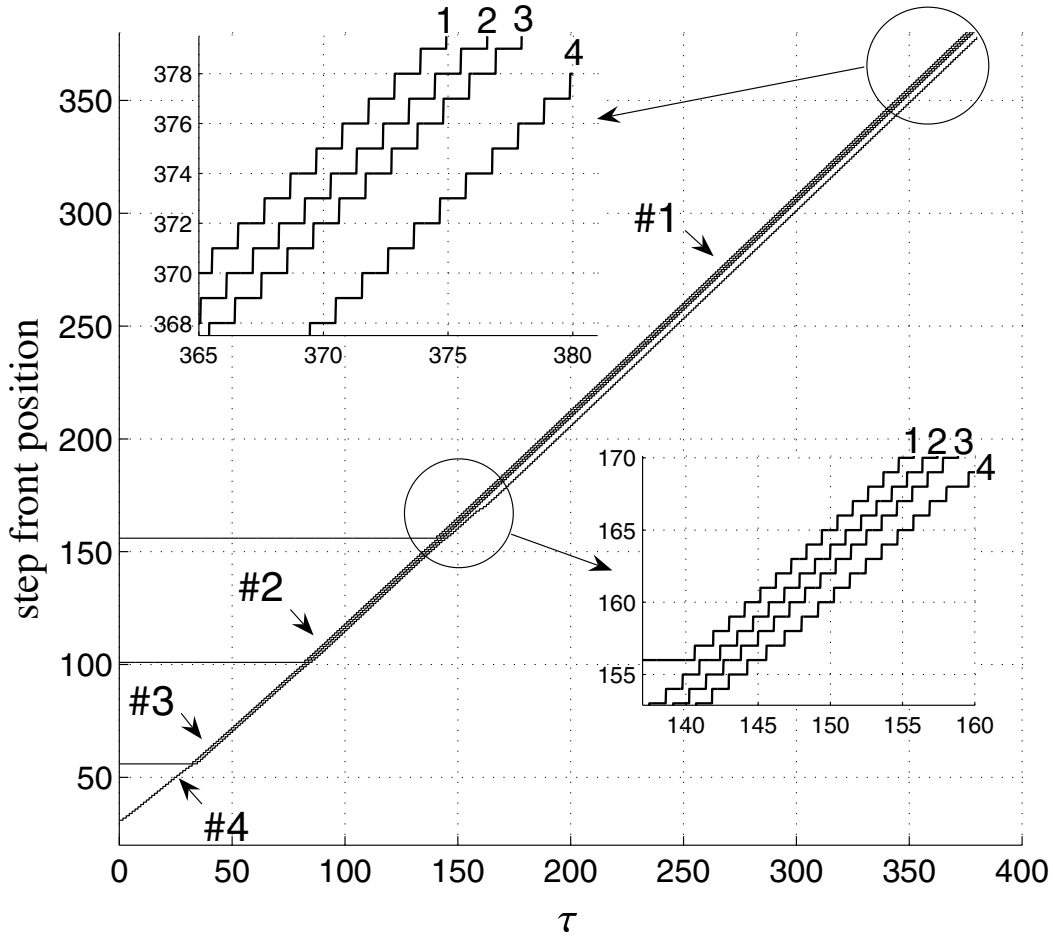


Fig. 12. The sequential motion of a four-step configuration with $v_- = 0.57$ on a computational domain of 400×10 . The steady motion has a velocity of $V/c = 0.9575$.

6 Cascade step nucleation

Our analysis in Part I predicted that when steps propagate at a speed above a certain critical value V_H , the steady motion breaks down. If the steps are either sufficiently close or well separated, this leads to periodic nucleation of islands of phase II on top of the existing step configuration and results a cascade step nucleation.

To demonstrate this important phenomenon, consider an initial configuration with a single step. When a sufficiently high driving force is applied, the step starts moving supersonically ($V > c$). See, for example, Fig. 14, where a case with $v_- = 0.595$ is shown. After an initial transient time, the step moves steadily with $V/c = 1.0204$ until $\tau \approx 13.5$. At this point a new island of vertical bonds in phase II nucleates on top of the existing step #1, as shown in Fig. 15. The island (denoted as #2 in Fig. 14) then starts growing, with its right and left boundaries moving forward and backward, respectively. Note

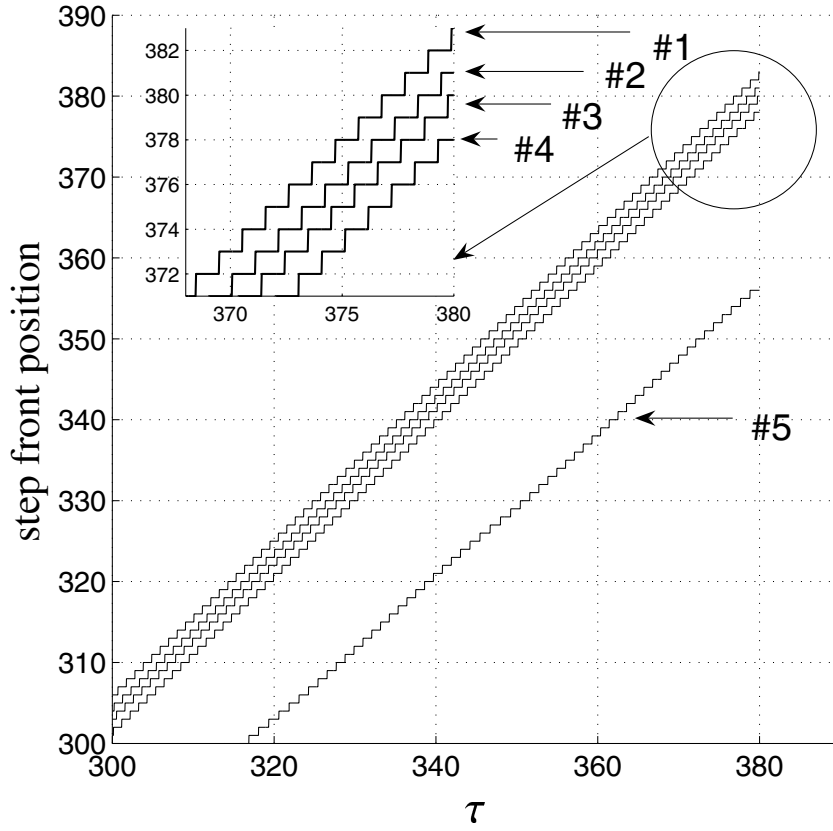


Fig. 13. The sequential motion of a five-step configuration with $v_- = 0.57$ on a computational domain of 400×11 . Only the late stage is depicted. The steady motion of the subgroup #1 to #4 has a velocity of $V/c = 0.9615$.

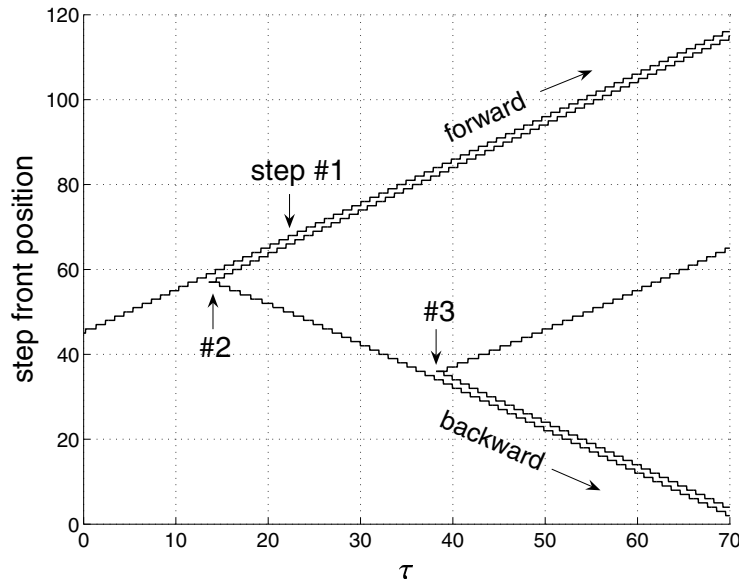


Fig. 14. Step nucleation and supersonic sequential motion with $V/c = 1.0204$. Here $v_- = 0.595$, and the initial configuration has a single step. New islands #2 and #3 are generated consecutively on top of #1 and #2.

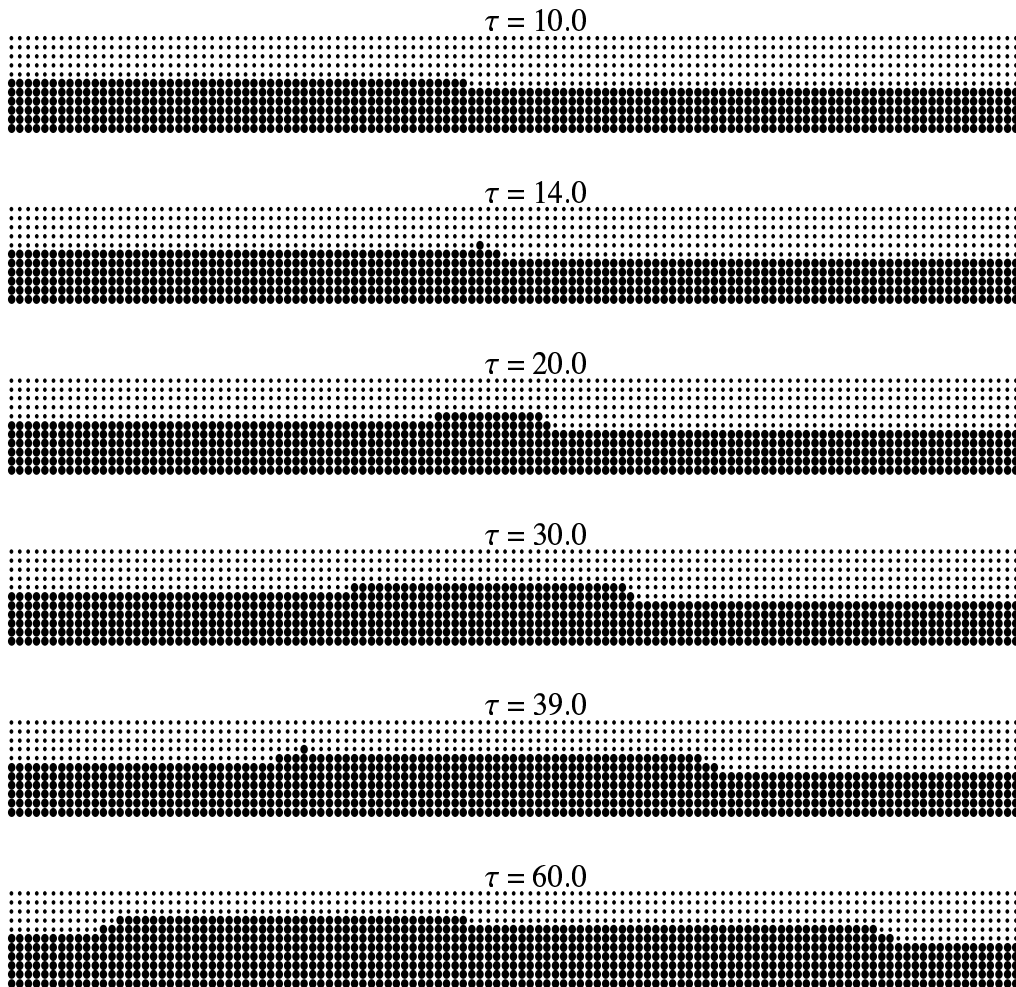


Fig. 15. Island nucleation and growth. The time snapshots correspond to the simulations shown in Fig. 14 ($v_- = 0.595$). Vertical bonds in the black region are in phase II, and the grey region contains phase I bonds.

that the forward moving front of the island now moves alternately with step #1 at the same velocity, with parameters of $\mu = 1$ and $T_1 = 0.28$ ($\alpha = 1.7143$), while the other boundary moves in the opposite direction at approximately the same speed. The parameters of the alternate motion agree well with those predicted in Figs. 5 and 6 of Part I, which yield $V/c = 1.023$ and $\alpha = 1.7059$. At $\tau \approx 38$ a new island (#3) nucleates on top of the existing ones (see Fig. 15), and the backward moving fronts of the two islands (#2 and #3) start moving in an alternate style, while the forward moving front of the new island (step #3) propagates alone.

The front position plots at applied strains $v_- = 0.6, 0.61, 0.62$ and 0.63 are shown in Fig. 16. The corresponding velocities are $V/c \approx 1.048, 1.119, 1.230$ and 1.433 . As the applied force increases, the new islands are nucleated more frequently, and several islands may nucleate in the same row of vertical bonds.

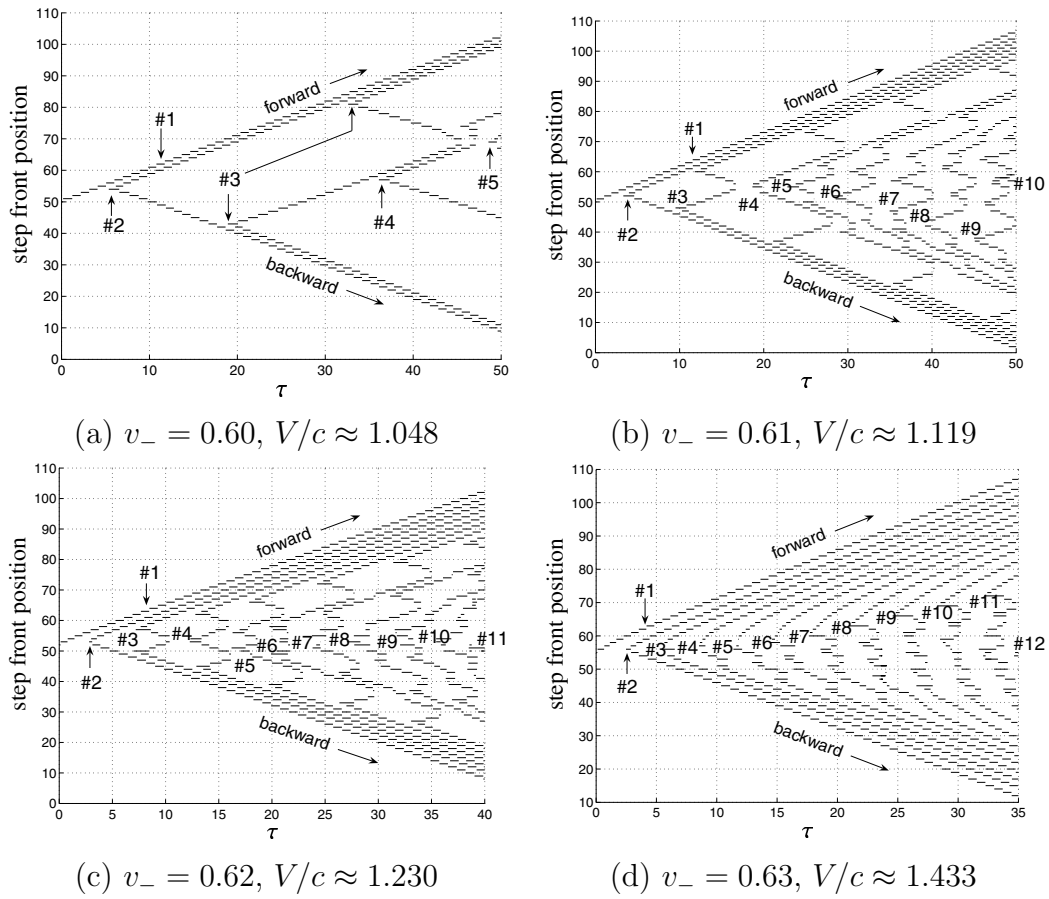


Fig. 16. Step nucleation and supersonic sequential motion under different applied loading. The initial configuration has a single step.

For example, at $v_- = 0.6$ and $\tau = 33$ a new island is nucleated in the same row and to the right of the existing one, as shown in Fig. 17. The left boundary of this new island propagates to the left, while the right boundary of the existing island in the same row continues moving to the right, until the two islands merge at $\tau \approx 45.5$. Meanwhile, the right boundary of the island forms a sequentially moving group with two other forward moving fronts on neighboring rows. See Fig. 16(a) for the corresponding front position plot.

While the above cases show the cascade nucleation at supersonic speeds, our analysis in Part I suggests that subsonic nucleation is also possible, provided that χ is sufficiently small. To check this, we conducted simulations at $\chi = 0.7$ and 0.8 on a domain of 17×200 with $v_- = 0.588$. The results show that for a single-step initial configuration, subsonic nucleation occurs for both $\chi = 0.7$ (with $V/c = 0.9924$) and $\chi = 0.8$ (with $V/c = 0.9923$). With the exception of the step velocity, the plots are similar to the cases of supersonic nucleation presented above.

The cascade step nucleation we observe is similar to the nucleation of multiple screw dislocations observed in the numerical simulations of Koizumi et al.

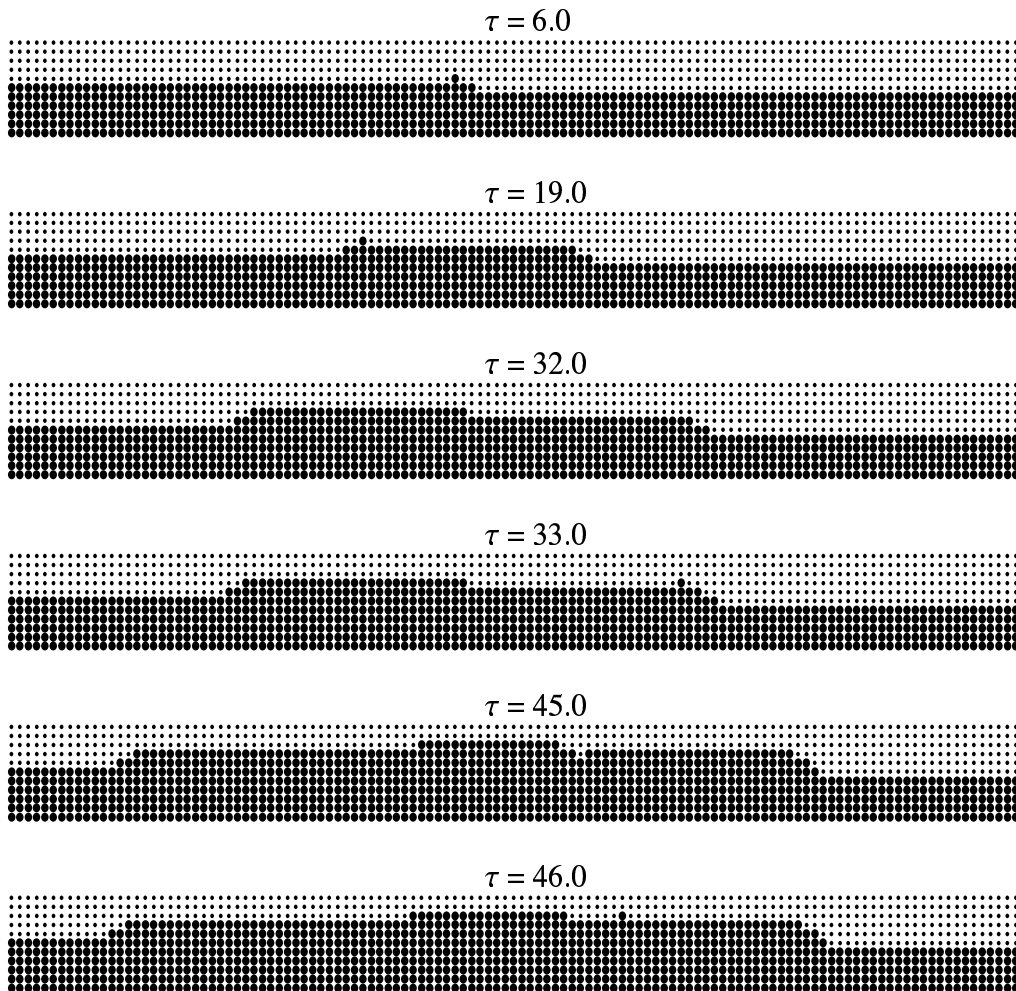


Fig. 17. Nucleation, growth and coalescence of islands. The time snapshots correspond to the simulations shown in Fig. 16(a) ($v_- = 0.60$).

(2002). There are, however, some important differences. First, the onset of instability of a moving dislocation and creation of a dislocation pair takes place at much lower subsonic critical speed: $V_H \approx 0.7c$ for the nonlinear periodic potential used in Koizumi et al. (2002); the calculations in Flytzanis et al. (1974) suggest a higher value, $V_H \approx 0.95c$, for a periodic potential with quadratic wells, while a comparable case ($\chi = 1$) in our model yields a nearly sonic critical speed, $V_H = 0.998c$. The apparent stabilization of the subsonic regime is due to the three-parabola potential used in the present model which prevents the vertical bonds that have already changed phase from making a reverse transition under continued loading. The island nucleation does not take place until the strain oscillations due to lattice waves in the wake of the moving step become sufficiently large to cause the neighboring bonds above the step to switch to the higher-strain phase. Meanwhile, periodic potentials used to model screw dislocations result in a different breakdown mechanism of sufficiently fast subsonic motion (Flytzanis et al., 1974), as explained in Part I.

In addition, in the simulations of Koizumi et al. (2002) most new dislocations form on the same slip plane as the original one, while here the new islands grow on top of the existing ones. This is analogous to formation of dislocation pairs on the consecutive slip planes, as predicted in the twinning model of Ishioka (1975).

The inclusion of anisotropy in our model allowed us to see that the value of the critical velocity V_H marking the onset of step nucleation depends on the anisotropy parameter χ and becomes supersonic at sufficiently high χ (see Tables 1 and 2 in Part I), so that a stable supersonic step motion becomes possible, as described in Section 4.3. Such motion was not observed in Koizumi et al. (2002).

7 Concluding remarks

In this work we have performed numerical simulations to study the dynamics of a group of steps along a phase boundary. The simulation results verify stability of solutions with sequential step motion derived in Part I for at least a sufficiently small number of neighboring steps. We show that at a given applied force multiple solutions of this type can coexist. The solutions have different step separations, time delays and velocities and are selected by the initial condition. Our model also accounts for lattice anisotropy, and its effects are investigated analytically and numerically.

To eliminate spurious reflections of elastic waves from the boundaries of the computational domain and focus on the intrinsic kinetics of the moving steps, we have derived a Kirchhoff-type exact non-reflecting boundary condition and devised a fast algorithm for its evaluation. This allows us to compare the sequential step motion obtained in the simulations to the analytical solutions derived in Part I. The comparison yields an excellent agreement.

An interesting phenomenon revealed by our simulations is the cascade step nucleation. When the steps move with velocity above a certain critical value V_H predicted in Part I, islands of phase II nucleate on top of the existing step configuration in a cascade manner. The nucleated steps move forward and backward, joining the existing steps and forming sequentially moving groups. Step nucleation is triggered when the magnitude of lattice waves emitted by the moving front becomes sufficiently large, causing the bonds above the steps to change phase. The dependence of V_H on elastic anisotropy χ presented in Part I are verified numerically by the presence of its two consequences: first, subsonic step nucleation occurs for weaker harmonic bonds; and second, the steady supersonic sequential motion of steps at $V < V_H$.

In the future work we will consider more realistic interaction potentials with different elastic moduli in the two phases and a non-degenerate spinodal region, the nonconvex region between the two phases. Preliminary simulations with a narrow spinodal region show very similar results but the effect of the width of the spinodal region needs to be further investigated. Finding analytical solutions when the interaction potential has a non-degenerate spinodal region remains an open problem, even for piecewise quadratic potentials, but the case of bilinear bonds with different elastic moduli can be handled analytically. Another interesting case to consider both numerically and analytically is that of a triangular lattice. We also plan to conduct simulations of step motion assuming fully nonlinear potentials, plane strain and three-dimensional deformation and non-zero temperature.

Along with previous work on Hamiltonian lattice models, the present study suggests that steady motion of lattice defects can only occur at sufficiently high velocities. Understanding what type of nonsteady motion takes place at lower average velocities remains a challenge left for future investigations.

Acknowledgements

This work was supported by the NSF grant DMS-0443928 (A.V.).

A Equilibrium step configuration and Peierls force

The non-reflecting boundary condition derived in Section 2 requires an equilibrium solution in the outer domain \mathcal{D} . This static solution contains the effect of the flat steps on the left and right side of the computational domain Ω . Note that the essential inputs to the NRBC are the displacements on \mathcal{S} and \mathcal{S}^+ .

The equilibrium equations for an N -step configuration in a lattice with bilinear vertical bonds are

$$\begin{aligned} \chi(u_{m+1,n} + u_{m-1,n} - 2u_{m,n}) + (u_{m,n+1} + u_{m,n-1} - 2u_{m,n}) = \\ - a \left[\delta_{n,1-N} + \sum_{p=0}^{N-1} (\delta_{n,1-p} - \delta_{n,-p}) \rho(m - \mu_p) \right], \quad (\text{A.1}) \end{aligned}$$

where μ_p (an integer) is the distance between the N th and $(N-p)$ th steps (thus $\mu_0 = 0$), $\delta_{m,n}$ is the Kronecker delta function and $\rho(x)$ is the complementary unit step function ($\rho(x) = 1$ for $x < 0$ and $\rho(x) = 0$ otherwise). The solution

of Eq. (A.1) can be written as

$$u_{m,n} = u_n^F + u_{m,n}^C, \quad (\text{A.2})$$

where

$$u_n^F = \begin{cases} (n-1+N)(v_- - a), & n \geq 1-N, \\ (n-1+N)v_-, & n \leq -N \end{cases} \quad (\text{A.3})$$

is the solution to the flat phase boundary problem with the right hand side given by $-a\delta_{n,1-N}$, and $u_{m,n}^C$ is the solution due to remaining terms. Note that for each p the term $-a(\delta_{n,1-p} - \delta_{n,-p})\rho(m - \mu_p)$ corresponds to a series of dipole sources locating at $(m, (1-p))$ and $(m, -p)$ with magnitude of $\pm a$, respectively, where m runs from $-\infty$ to μ_p . Using the lattice Green's function (Cserti, 2000)

$$\Gamma_{m,n} = \frac{1}{\pi\chi} \int_0^\pi \frac{\exp(-|m|s) \cos k_y n}{2 \sinh s} dk_y, \quad (\text{A.4})$$

which satisfies

$$\chi(\Gamma_{m+1,n} + \Gamma_{m-1,n} - 2\Gamma_{m,n}) + (\Gamma_{m,n+1} + \Gamma_{m,n-1} - 2\Gamma_{m,n}) = -\delta_{m,0}\delta_{n,0}, \quad (\text{A.5})$$

we obtain

$$u_{m,n}^C = \frac{a}{\pi\chi} \sum_{p=0}^{N-1} \sum_{j=-\infty}^{\mu_p} \int_0^\pi \frac{\exp(-|m-j|s)(\cos k_y(n+p-1) - \cos k_y(n+p))}{2 \sinh s} dk_y. \quad (\text{A.6})$$

Here $s \geq 0$ satisfies $\cosh s = (\chi + 1 - \cos k_y)/\chi$. The integral over k_y in Eq. (A.6) can be evaluated numerically by using the fact that

$$\sum_{j=-\infty}^{\mu_p} \exp(-|m-j|s) = \begin{cases} \frac{1 + \exp(-s)(1 - \exp(-s(\mu_p - m)))}{1 - \exp(-s)}, & m < \mu_p, \\ \frac{\exp(-s(m - \mu_p))}{1 - \exp(-s)}, & m \geq \mu_p. \end{cases} \quad (\text{A.7})$$

The equilibrium solution is valid as long as the vertical strains $v_{m,n}$ remain in their respective phases. This sets constraints on the far-field strain v_- and thus the corresponding driving force $G = a(v_- - v_c - a/2)$ as well. One can show that only for $|G|$ below a certain threshold value G_P called the Peierls force, which can be determined by the above constraints, the solution exists and is stable. To illustrate this, we will use a single-step case in the following derivation.

For a single step configuration, the vertical strain for the equilibrium state reduces to

$$v_{m,n} = \frac{a}{\pi} \int_0^\pi \mathcal{I}(m) \frac{\cosh s - 1}{\sinh s} \cos k_y(n-1) dk_y + \begin{cases} v_- - a, & n \geq 1, \\ v_-, & n \leq 0, \end{cases} \quad (\text{A.8})$$

where $\mathcal{J}(m)$ is given by

$$\mathcal{J}(m) = \begin{cases} \frac{1 + \exp(-s)(1 - \exp(ms))}{1 - \exp(-s)}, & m < 0, \\ \frac{\exp(-ms)}{1 - \exp(-s)}, & m \geq 0. \end{cases} \quad (\text{A.9})$$

The requirement that vertical bonds remain in their respective phases reduces to the inequalities

$$\begin{aligned} v(0, 1) &= v_- + a \left(\frac{1}{\pi} \int_0^\pi \frac{1}{1 - \exp(-s)} \frac{\cosh s - 1}{\sinh s} dk_y - 1 \right) > v_c, \\ v(1, 1) &= v_- - a \left(\frac{1}{\pi} \int_0^\pi \frac{\exp(-s)}{1 - \exp(-s)} \frac{\cosh s - 1}{\sinh s} dk_y - 1 \right) < v_c. \end{aligned} \quad (\text{A.10})$$

These constraints imply that $-G_P < G < G_P$, where

$$G_P = a^2 \left(\frac{1}{2} - \frac{1}{\pi} \int_0^\pi \frac{\exp(-s)}{1 - \exp(-s)} \frac{\cosh s - 1}{\sinh s} dk_y \right) \quad (\text{A.11})$$

is the Peierls force. The interval $[-G_P, G_P]$ of driving forces for which a stable static solution exists is called the trapping region. At $\chi = 1$, the Peierls force (A.11) can be evaluated exactly, where we obtain

$$G_P = \frac{a^2}{4}. \quad (\text{A.12})$$

For the values $v_c = 0.42$ and $a = 0.22$ used in the simulations, this yields $G_P = 0.0121$ and the corresponding $v_-^P = 0.585$. Above this threshold level the equilibrium state no longer exists and we expect to see a stable dynamic solution. This is consistent with the numerical simulation results presented in the current work.

References

- Adelman, S., Doll, J., 1974. Generalized Langevin equation approach for atom/solid-surface scattering: collinear atom/harmonic chain model. *J. Chem. Phys.* 61, 4242–4245.
- Bayliss, A., Turkel, E., 1980. Radiation boundary conditions for wave-like equations. *Comm. Pure Appl. Math.* 33, 707–725.
- Cai, W., Koning, M., Bulatov, V., Yip, S., 2000. Minimizing boundary reflections in coupled-domain simulations. *Phys. Rev. Lett.* 85 (15), 3213–3216.
- Cserti, J., 2000. Application of the lattice Green’s function for calculating the resistance of infinite networks of resistors. *American J. Phys.* 68, 896–906.
- Engquist, B., Majda, A., 1977. Absorbing boundary conditions for the numerical simulation of waves. *Math. Comp.* 31, 629–651.

- Engquist, B., Majda, A., 1979. Absorbing boundary conditions for acoustic and elastic wave calculations. *Comm. Pure Appl. Math.* 32, 313–357.
- Flytzanis, N., Celli, V., Nobile, A., 1974. Motion of two screw dislocations in a lattice. *J. Appl. Phys.* 45 (12), 5176–5181.
- Givoli, D., 1991. Non-reflecting boundary conditions. *J. Comput. Phys.* 94, 1–29.
- Givoli, D., 1999. Exact representations on artificial interfaces and applications in mechanics. *Appl. Mech. Rev.* 52, 333–349.
- Glasser, M., Boersma, J., 2000. Exact values for the cubic lattice Green functions. *J. Phys. A: Math. Gen.* 33, 5017–5023.
- Grote, M., Keller, J., 1995a. Exact nonreflecting boundary conditions for the time dependent wave equation. *SIAM J. Appl. Math.* 55 (2), 280–297.
- Grote, M., Keller, J., 1995b. On nonreflecting boundary conditions. *J. Comput. Phys.* 122, 231–243.
- Hagstrom, T., 1999. Radiation boundary conditions for the numerical simulation of waves. In: Iserles, A. (Ed.), *Acta Numerica*. Vol. 8. Cambridge University Press, Cambridge, pp. 47–106.
- Higdon, R. L., 1986. Absorbing boundary conditions for difference approximations to the multi-dimensional wave equation. *Math. Comp.* 47 (176), 437–459.
- Higdon, R. L., 1990. Radiation boundary conditions for elastic wave propagations. *SIAM J. Numer. Anal.* 27 (4), 831–870.
- Ishioka, S., 1975. Stress field around a high speed screw dislocation. *J. Phys. Chem. Solids* 36, 427–430.
- Karpov, E., Wagner, G., Liu, W., 2005. A Green’s function approach to deriving non-reflecting boundary conditions in molecular dynamics simulations. *Int. J. Numer. Methods Engrg.* 62 (9), 1250–1262.
- Katsura, S., Inawashiro, S., 1971. Lattice Green’s functions for the rectangular and the square lattices at arbitrary points. *J. Math. Phys.* 12 (8), 1622–1630.
- Katsura, S., Morita, T., Inawashiro, S., Horiguchi, T., Abe, Y., 1971. Lattice Green’s function. introduction. *J. Math. Phys.* 12 (5), 892–895.
- Koizumi, H., Kirchner, H., Suzuki, T., 2002. Lattice waves emission from a moving dislocation. *Phys. Rev. B* 65, 214104.
- Li, X., E, W., 2006. Variational boundary conditions for molecular dynamics simulations of solids at low temperature. *Comm. Comput. Phys.* 1 (1), 135–175.
- Lubich, C., Schädle, A., 2002. Fast convolution for nonreflecting boundary conditions. *SIAM J. Sci. Comput.* 24 (1), 161–182.
- Morita, T., 1971. Useful procedure for computing the lattice Green’s function — square, tetragonal, and bcc lattices. *J. Math. Phys.* 12 (8), 1744–1747.
- Murli, A., Rizzardi, M., 1990. ALGORITHM 682: Talbot’s method for the laplace inversion problem. *ACM Trans. Math. Soft.* 16 (2), 158–168.
- Park, H., Karpov, E., Liu, W., Klein, P., 2005. The bridging scale for two-dimensional atomistic/continuum coupling. *Philos. Mag.* 85, 79–113.
- Ryaben’kii, V., Tsynkov, S., Turchaninov, V., 2001. Global discrete artifi-

- cial boundary conditions for time-dependent wave propagation. *J. Comput. Phys.* 174, 712–758.
- Teng, Z.-H., 2003. Exact boundary condition for time-dependent wave equation based on boundary integral. *J. Comput. Phys.* 190, 398–418.
- Tewary, V., 1995. Computationally efficient representation for elastostatic and elastodynamic Green’s functions for anisotropic solids. *Phys. Rev. B* 51 (22), 15695–15702.
- Tsynkov, S., 1998. Numerical solution of problems on unbounded domains. a review. *Appl. Numer. Math.* 27, 465–532.
- Wagner, G., Karpov, E., Liu, W., 2004. Molecular dynamics boundary conditions for regular crystal lattice. *Comput. Method Appl. Mech. Engrg.* 193, 1579–1601.
- Zhen, Y., Vainchtein, A., 2007. Dynamics of steps along a martensitic phase boundary I: Semi-analytical solution. *Journal of the Mechanics and Physics of Solids* (submitted).